Ring artifact correction using detector line-ratios in computed tomography

Younguk Kim,[1] Jongduk Baek,[2] and Dosik Hwang[1,*]

[1]*School of Electrical and Electronic Engineering, Yonsei University, Seoul 120-749, South Korea*
[2]*School of Integrated Technology, Yonsei University, Incheon, 406-840, South Korea*
[*]*dosik.hwang@yonsei.ac.kr*

Abstract: Ring artifacts in computed tomography (CT) images degrade image quality and obscure the true shapes of objects. While several correction methods have been developed, their performances are often task-dependent and not generally applicable. Here, we propose a novel method to reduce ring artifacts by calculating the ratio of adjacent detector elements in the projection data, termed the line-ratio. Our method estimates the sensitivity of each detector element and equalizes them in sinogram space. As a result, the stripe pattern can be effectively removed from sinogram data, thereby also removing ring artifacts from the reconstructed CT image. Numerical simulations were performed to evaluate and compare the performance of our method with that of conventional methods. We also tested our method experimentally and demonstrated that our method has superior performance to other methods.

OCIS codes: (170.3880) Medical and biological imaging; (170.6960) Tomography.

References and links

1. J. J. Liu, S. R. Watt-Smith, and S. M. Smith, "A description for computed tomography based on sinusoidal curves," J. XRay Sci. Technol. **11**(4), 205–218 (2003).
2. P. Rüegsegger, B. Koller, and R. Müller, "A microtomographic system for the nondestructive evaluation of bone architecture," Calcif. Tissue Int. **58**(1), 24–29 (1996).
3. J. T. Dobbins 3rd and D. J. Godfrey, "Digital X-ray tomosynthesis: current state of the art and clinical potential," Phys. Med. Biol. **48**(19), R65–R106 (2003).
4. V. Cnudde, B. Masschaele, M. Dierick, J. Vlassenbroeck, L. V. Hoorebeke, and P. Jacobs, "Recent progress in X-ray CT as a geosciences tool," Appl. Geochem. **21**(5), 826–832 (2006).
5. G. L. Zeng, "Nonuniform noise propagation by using the ramp filter in fan-beam computed tomography," IEEE Trans. Med. Imaging **23**(6), 690–695 (2004).
6. J. Hsieh, *Computed Tomography-Principles, Artifacts, and Recent Advances* (SPIE Publications, 2003).
7. J. A. Seibert, J. M. Boone, and K. K. Lindfors, "Flat-field correction technique for digital detectors," Proc. SPIE **3336**, *Medical Imaging 1998: Physics of Medical Imaging*, 348 (1998), pp. 348–354.
8. G. R. Davis and J. C. Elliott, "X-ray microtomography scanner using time-delay integration for elimination of ring artefacts in the reconstructed image," Nucl. Instrum. Meth. A. Equipment. **394**(1-2), 157–162 (1997).
9. C. Raven, "Numerical removal of ring artifacts in microtomography," Rev. Sci. Instrum. **69**(8), 2978–2980 (1998).
10. X. Tang, R. Ning, R. Yu, and D. Conover, "Cone beam volume CT image artifacts caused by defective cells in X-ray flat panel imagers and the artifact removal using a wavelet-analysis-based algorithm," Med. Phys. **28**(5), 812–825 (2001).
11. J. Sijbers and A. Postnov, "Reduction of ring artefacts in high resolution micro-CT reconstructions," Phys. Med. Biol. **49**(14), N247–N253 (2004).
12. M. Axelsson, S. Svensson, and G. Borgefors, "Reduction of ring artifacts in high resolution X-ray microtomography images," in *Lecture Notes in Computer Science,* Volume 4174 (Springer, 2006), pp. 61–70.
13. M. Boin and A. Haibel, "Compensation of ring artefacts in synchrotron tomographic images," Opt. Express **14**(25), 12071–12075 (2006).
14. R. A. Ketcham, "New algorithms for ring artifact removal," Proc. SPIE **6318**, 63180O (2006).
15. Y. Kyriakou, D. Prell, and W. A. Kalender, "Ring artifact correction for high-resolution micro CT," Phys. Med. Biol. **54**(17), N385–N391 (2009).
16. B. Münch, P. Trtik, F. Marone, and M. Stampanoni, "Stripe and ring artifact removal with combined wavelet--Fourier filtering," Opt. Express **17**(10), 8567–8591 (2009).
17. D. Prell, Y. Kyriakou, and W. A. Kalender, "Comparison of ring artifact correction methods for flat-detector CT," Phys. Med. Biol. **54**(12), 3881–3895 (2009).

#208844 - $15.00 USD Received 25 Mar 2014; revised 19 May 2014; accepted 20 May 2014; published 27 May 2014

18. E. M. Abu Anas, S. Y. Lee, and M. K. Hasan, "Removal of ring artifacts in CT imaging through detection and correction of stripes in the sinogram," Phys. Med. Biol. **55**(22), 6911–6930 (2010).
19. F. Sadi, S. Y. Lee, and M. K. Hasan, "Removal of ring artifacts in computed tomographic imaging using iterative center weighted median filter," Comput. Biol. Med. **40**(1), 109–118 (2010).
20. S. Titarenko, P. J. Withers, and A. Yagola, "An analytical formula for ring artefact suppression in X-ray tomography," Appl. Math. Lett. **23**(12), 1489–1495 (2010).
21. V. Titarenko, R. Bradley, C. Martin, P. J. Withers, and S. Titarenko, "Regularization methods for inverse problems in X-ray tomography," Proc. SPIE **7804**, *Developments in X-Ray Tomography VII*, 78040Z (2010).
22. E. M. Anas, J. G. Kim, S. Y. Lee, and K. Hasan, "Comparison of ring artifact removal methods using flat panel detector based CT images," Biomed. Eng. Online **10**(1), 72 (2011).
23. E. M. A. Anas, S. Y. Lee, and K. Hasan, "Classification of ring artifacts for their effective removal using type adaptive correction schemes," Comput. Biol. Med. **41**(6), 390–401 (2011).
24. E. M. A. Anas, J. Kim, S. Y. Lee, and M. K. Hasan, "Ring artifact corrections in flat-panel detector based cone beam CT," Proc. SPIE **7961**, *Medical Imaging 2011: Physics of Medical Imaging* (2011).
25. E. M. A. Anas, J. G. Kim, S. Y. Lee, and M. K. Hasan, "High-quality 3D correction of ring and radiant artifacts in flat panel detector-based cone beam volume CT imaging," Phys. Med. Biol. **56**(19), 6495–6519 (2011).
26. A. N. M. Ashrafuzzaman, S. Y. Lee, and M. K. Hasan, "A self-adaptive approach for the detection and correction of stripes in the sinogram: Suppression of ring artifacts in CT imaging," Eurasip. J. Adv. Sig. Pr. 2011 (2011).
27. F. Brun, G. Kourousias, D. Dreossi, L. Mancini, and G. Tromba, "A comparative evaluation of ring artifacts reduction filters for X-ray computed microtomography images," in *2011 18th IEEE International Conference on Image Processing (ICIP)* (IEEE, 2011), pp. 405–408.
28. S. Titarenko, V. Titarenko, A. Kyrieleis, P. J. Withers, and F. De Carlo, "Suppression of ring artefacts when tomographing anisotropically attenuating samples," J. Synchrotron Radiat. **18**(3), 427–435 (2011).
29. M. K. Hasan, F. Sadi, and S. Y. Lee, "Removal of ring artifacts in micro-CT imaging using iterative morphological filters," Signal. Image. Video. P. **6**, 41–53 (2012).
30. G. L. Zeng, *Medical Image Reconstruction: A Conceptual Tutorial* (Springer, 2010).
31. D. Library, "CT DICOM Samples," (DICOM Library, 2012), http://www.dicomlibrary.com/?study=1.2.826.0.1.3680043.8.1055.1.20111102150758591.92402465.76095170.
32. I. Avcibaş, B. Sankur, and K. Sayood, "Statistical evaluation of image quality measures," J. Electron. Imaging **11**(2), 206–223 (2002).

1. Introduction

Computed tomography (CT) is an imaging technique used to produce three-dimensional images from a two-dimensional projection data set [1]. CT has been used for various medical applications, including the diagnosis of cancers, organ defects, and various diseases. Moreover, CT is also used in industry to identify circuit defects, locate cracks in mechanical parts, and verify soldering completeness [2–4]. As CT becomes a valuable tool in medicine, industry, archaeology, and other fields, various types of CT artifacts will need to be effectively removed in order to produce useful reconstructed tomographic images [5]. One such example is the ring artifact, which is a CT artifact observed in both medical and nonmedical CT images whose presence is known to degrade image quality [6].

Charge-coupled devices (CCDs) and flat panel detectors (FPDs) are frequently used as X-ray detectors in many CT systems. However, uniform sensitivity of detector elements is hardly achievable; moreover, non-uniform detector sensitivity contributes to ring artifacts in reconstructed CT images. To compensate for these artifacts, the flat-field correction (FFC) method has been used [7]. In the FFC method, the non-uniformity of the detector elements is estimated and compensated for using flat-field data. Even though the FFC method can reduce ring artifacts to some extent, a substantial number of ring patterns still remain, due to imperfect measurements of the flat-field X-ray intensity and other object-dependent effects. Another method of reducing ring artifacts is to scan a known object, estimate the detector non-uniformity, and compensate for this non-uniformity. However, one drawback of this method is that different objects often require different measurement conditions, such as various tube voltages and collimator apertures [6].

Another class of ring artifact correction methods is made up of the post-processing methods, in which various signal-processing techniques are applied to the reconstructed images or the acquired projection data before reconstruction [8–29]. These post-processing approaches have been studied in two different domains: the image-domain and the sinogram-domain. In image-domain post-processing methods, the concentric ring patterns are estimated in the reconstructed images, and the estimated ring patterns are subtracted from these

#208844 - $15.00 USD Received 25 Mar 2014; revised 19 May 2014; accepted 20 May 2014; published 27 May 2014

reconstructed images. In sinogram-domain post-processing methods, the non-uniformity of the detector elements is estimated by processing the measured sinogram data. Then, the stripe patterns caused by element non-uniformity can be reduced based on these estimations. After reduction of stripe patterns, images are reconstructed to generate ring-artifact-compensated images. Both approaches result in substantial reduction of ring artifacts. However, image-domain methods process reconstructed images only after the artifacts have been generated. Thus, the performance of such methods can be limited by the artifacts inherent in Filtered Back-Projection (FBP) reconstruction, which cannot be easily detected and removed by post-processing in the image domain [7]. In contrast, sinogram-domain approaches process raw data before reconstruction, an approach by which ring artifacts can be removed more effectively. Thus, recent studies have focused on sinogram-domain approaches, such as low-pass or median filtering applications, on sinogram data to reduce ring artifacts [9, 14, 16, 19, 23–26, 28, 29].

However, conventional sinogram-domain methods do not always perform well; moreover, such methods usually need to be improved before they can be considered generally applicable. For example, conventional methods such as mean or median filtering of sinogram data demonstrate fundamental limitations caused by their filter properties. Since significant information is lost by both methods during the filtering process, conventional sinogram-domain methods may smooth detailed features in the original images, or introduce additional artifacts into the reconstructed images. Furthermore, ring artifacts may not be sufficiently reduced if the filter coefficients are not adequate [1, 2]. In order to overcome these problems, one study introduced an iterative method to adaptively reduce ring artifacts [3]; however, the iterative process described in that study needs object-dependent optimization.

In this paper, we propose a novel sinogram-domain-based ring artifact correction method. In this method, the non-uniform sensitivities of the detector elements are estimated using line-ratios, which are derived from the individual detector elements. These estimated line-ratios are applied to each element, thereby reducing the stripe patterns in the sinogram data. This method effectively equalizes the sensitivities of all detector elements, which removes the stripe patterns from the sinogram data and reduces the amount of ring artifacts in the reconstructed CT image. We performed numerical simulations to evaluate the performance of our method, and compared its performance with that of conventional methods. Our method was also tested with experimental data.

2. Concept and implementation

2.1. Cause of ring artifacts

Identical detector elements are virtually impossible to manufacture. For example, detector elements cannot be cut in batches of equal size. In addition, the surface roughness of detector elements varies according to the treatment process. Photodiodes connected to scintillator cells may vary in spectral response and conversion efficiency. Cumulatively, all of these differences result in different gains for each detector element. These differences can be modeled in the following equation (Eq. (1) [2, 4]:

$$D(t,\varphi) = F(t,\varphi) \cdot E(t) \tag{1}$$

where D is the distorted sinogram data, F is the ideal sinogram data with perfect uniformity of detector elements, E is the error due to the different gain of each detector element as described above, t represents the location of each detector element in the detector space or each row in the sinogram data, and φ is the projection angle.

Since E is a function of t and does not depend on φ, the non-uniform sensitivity of the detector bins manifests itself as a stripe pattern in the sinogram data, $D(t, \varphi)$. Therefore, E can be efficiently estimated by the line-ratio method. Here, we focus on cases in which F can be estimated by D/E. However, it is also possible that several detector elements can also be completely broken. In this case, D does not depend on F due to severe defectiveness or hysteresis. Here, the detectors should be repaired or replaced to prevent ring artifacts.

#208844 - $15.00 USD Received 25 Mar 2014; revised 19 May 2014; accepted 20 May 2014; published 27 May 2014

Interpolation using adjacent bins may be incorporated, but this situation is not taken into account in this paper.

2.2 Basic idea

Data measured by ideal detectors with perfect uniformity depend only on the densities and shapes of the objects to be imaged. Therefore, the ratios of the adjacent detector elements depend only on the objects defined in Eq. (2), and the expected average ratio of all projection angles is close to 1 (Eq. (3), since the different ratios at different projection angles compensate for one another. Figure 1 shows that the wide range of individual ratios in (c) becomes close to 1 in (e) when averaged over all projection angles. (Exception occurs at the end of the object where projection values become zero. To factor out this exception, the expected ratios can be obtained by the median ratios as shown in (f).)

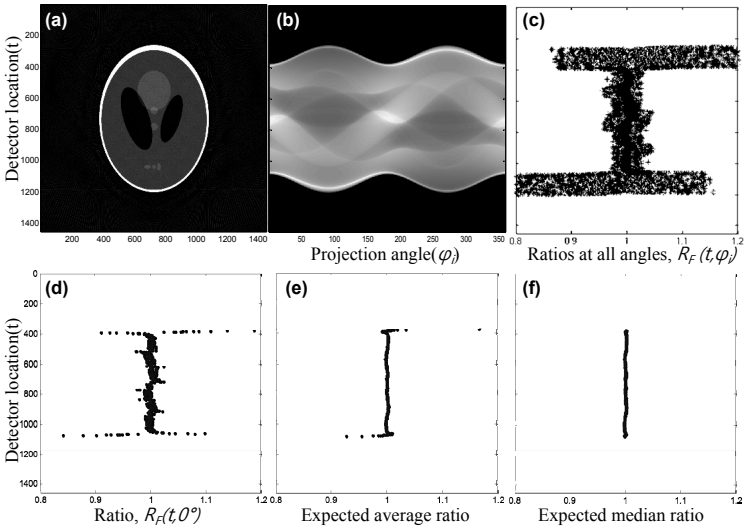

Fig. 1. The simulation study about the expected average and median ratios. (a) Shepp-Logan phantom, (b) ideal sinogram, (c) distribution of all ratios of the adjacent detector elements, (d) the ratios at a specific projection angle of 0 degree, (e) the expected average ratios, (f) the expected median ratios. The expected ratios are close to 1.

$$R_F(t,\varphi)=\frac{F(t+1,\varphi)}{F(t,\varphi)} \tag{2}$$

$$\frac{1}{M}\sum_{i=1}^{M}R_F(t,\varphi_i)=\frac{1}{M}\sum_{i=1}^{M}\frac{F(t+1,\varphi_i)}{F(t,\varphi_i)}\approx 1 \tag{3}$$

where $R_F(t,\varphi)$ is the ratio between projections at the uniform-sensitivity detector elements, t and $t+1$, at a specific angle, φ, and M is the total number of projection angles.

In contrast, for detectors with non-uniform sensitivity, the ratio of measured values in adjacent detector elements can be calculated by Eq. (4):

$$R(t,\varphi)=\frac{D(t+1,\varphi)}{D(t,\varphi)}=\frac{F(t+1,\varphi)\cdot E(t+1)}{F(t,\varphi)\cdot E(t)} \tag{4}$$

#208844 - $15.00 USD Received 25 Mar 2014; revised 19 May 2014; accepted 20 May 2014; published 27 May 2014

$$\begin{aligned}\frac{1}{M}\sum_{i=1}^{M}R(t,\varphi_i) &= \frac{1}{M}\sum_{i=1}^{M}\frac{D(t+1,\varphi_i)}{D(t,\varphi_i)}\\ &= \frac{1}{M}\sum_{i=1}^{M}\frac{F(t+1,\varphi_i)\cdot E(t+1)}{F(t,\varphi_i)\cdot E(t)}\\ &= \frac{E(t+1)}{E(t)}\frac{1}{M}\sum_{i=1}^{M}\frac{F(t+1,\varphi_i)}{F(t,\varphi_i)}\\ &\approx \frac{E(t+1)}{E(t)}\end{aligned} \tag{5}$$

This equation factors in the effect of non-uniform sensitivity, and the expected average ratio over all projection angles maintains the sensitivity difference between the two detector elements. The difference is maintained because the sensitivity difference between the detector elements is the same over all projection angles, as represented in Eq. (5). Therefore, the sensitivity difference between adjacent detector elements can be extracted from the ratios along all projection angles. This can be done by taking the expected average ratio, or some modified version of this ratio that best represents the sensitivity difference. This ratio will hereafter be referred to as the representative ratio.

2.3. Methods

2.3.1. Sensitivity difference estimation

To estimate the sensitivity differences between the detector elements, the representative ratio can be calculated from all ratios, as detailed in Eq. (5). For example, the mean or median values of all ratios can be calculated. However, some of the ratios at certain angles may be too large, not because of a sensitivity difference, but because the density difference of the original objects in the sinogram led to a biased estimation of the representative ratio. Therefore, these large ratios should not be included in the calculation of the representative ratio. We found that relatively large values in the sinogram tended to result in large ratios between adjacent detector elements, which were more influenced by the density difference of the objects, rather than by the sensitivity difference of detector elements. Therefore, only values less than a certain threshold in the sinogram were included for the calculation of the representative ratio. Each threshold for each detector element, $T(t)$, was determined by the median value of all $D(t, \varphi)$ values over all projection angles. Therefore, the selected set of $R_s(t, \varphi)$ was determined as in Eq. (6):

$$R_s(t,\varphi) = \{x \in R(t,\varphi) \mid D(t,\varphi) < T(t)\} \quad (t = 1,2,\cdots\cdots N) \tag{6}$$

The representative ratio $R_m(t)$ is now determined by the median of $R_s(t, \varphi)$.

$$R_m(t) = median(R_s(t,\varphi)) \tag{7}$$

$R_m(t)$ can be used as a correction factor to compensate for the sensitivity difference between two adjacent detector elements, t and $t + 1$. Moreover, $R_m(t)$ can be applied to all elements for all t, in a cascading way, to compensate for all sensitivity differences.

2.3.2. Correction factor

Correction factors for all detector elements can also be estimated from $R_m(t)$. All detector elements are numbered from 1 to N, and the representative ratio of the sensitivity between the (N-1)th and Nth detector elements becomes $R_m(N\text{-}1)$. Likewise, the ratio of sensitivity between the (N-2)th and (N-1)th detector elements can be represented as $R_m(N\text{-}2)$. By using these two ratios, the ratio of sensitivity between the (N-2)th and Nth detector elements can also be obtained by multiplying $R_m(N\text{-}1)$ with $R_m(N\text{-}2)$. Therefore, for an arbitrary detector

#208844 - $15.00 USD Received 25 Mar 2014; revised 19 May 2014; accepted 20 May 2014; published 27 May 2014

element, t, the sensitivity ratio can be represented as $R_m(N\text{-}1)\cdot R_m(N\text{-}2)\cdots\cdots R_m(N\text{-}t)$, as described in Eq. (8):

$$C(t)=\begin{cases}\prod_{i=1}^{N-t} R_m(N-i) & (1\le t\le N-1)\\ 1 & (t=N)\end{cases} \tag{8}$$

In this instance, $C(t)$ is the correction factor and can be applied to equalize the sensitivity of the detector elements. In some cases, $C(t)$ may contain some degree of object dependency that is not related to the sensitivity. Since this object dependency manifests as low frequency components in $C(t)$, a simple high pass filtering step can be applied to $C(t)$ to remove its object dependency and obtain the final correction factor, $C_f(t)$.

Finally, the corrected sinogram data, $\overline{D}$, are obtained by multiplying each projection data set by $C_f(t)$, as detailed in Eq. (9):

$$\overline{D}(t,\varphi)=C_f(t)\cdot D(t,\varphi) \tag{9}$$

A ring-free image can now be reconstructed from this corrected sinogram. The entire process for ring artifact removal is shown in Fig. 2.

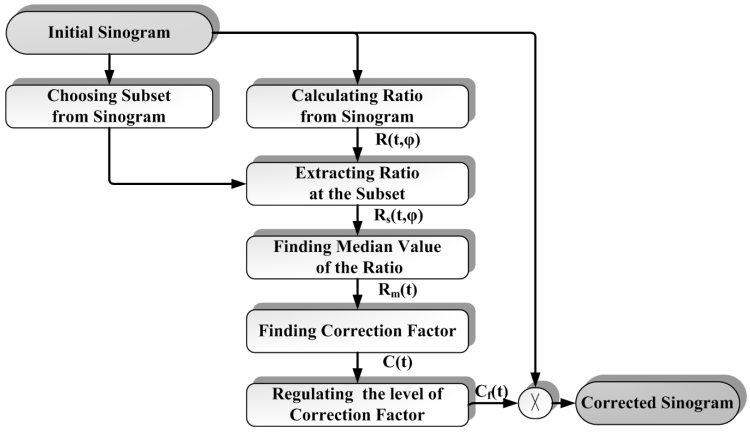

Fig. 2. Flow chart of the line-ratio-based ring artifact removal algorithm.

3. Simulations and experiments

To evaluate the performance of our ring artifact removal algorithm, we used both numerical simulation CT data and real CT data. Numerical simulation CT data exhibiting various ring patterns were generated; in addition, real CT data were also obtained. We compared our proposed method with two other conventional methods, the moving average (MA) method [13] and the median filtering (MedF) method [14]. The same reconstruction algorithm, the FBP algorithm with the Ram-Lak filter, was used for reconstruction from the corrected sinograms [30].

3.1. Simulation data

To validate the performance of our method, we designed an experiment with simulation data. A sinogram was generated from these simulation data by using numerical phantoms and applying a radon transform. Using the appropriate reconstruction algorithms, an ideal image with no artifacts was obtained. Then, the sensitivities of some of the detector elements were altered to produce ring artifacts. Here, we used three synthetic phantoms to simulate the ring artifact removal process.

Synthetic phantom 1 was the numerical Shepp-Logan phantom, as shown in Fig. 3(a). After performing a radon transform step to generate the sinogram, some detector elements

#208844 - $15.00 USD Received 25 Mar 2014; revised 19 May 2014; accepted 20 May 2014; published 27 May 2014

were randomly amplified to generate noise-free stripes in the sinogram. This distorted sinogram was then reconstructed into an image with ring artifacts, as shown in Fig. 3(b). In Figs. 4 and 5, the images resulting from synthetic phantoms 2 and 3, respectively, are shown. Synthetic phantom 2 was modeled after human organs, and synthetic phantom 3 was created from an actual CT image [31]. These synthetic phantoms were also tested with the same process used to add ring artifacts in synthetic phantom 1.

The resolution of all synthetic phantoms was 1024×1024 pixels, and the projection data from the synthetic phantoms yielded 360 degree views, from 0 to 359 degrees. The MA, MedF, and line-ratio methods were applied to all synthetic sinograms, with dimensions of 1024×360 matrices. The kernel sizes for the MA and MedF methods were 11 pixels and 7 pixels, respectively.

To quantitatively compare the results generated by the three algorithms, the Mean Square Error (MSE), a measurement which describes the difference between the ground-true image and each corrected image, was calculated using Eq. (10) [32]:

$$MSE = \frac{1}{mn} \sum_{i=0}^{m-1} \sum_{j=0}^{n-1} [I_o(i,j) - \hat{I}(i,j)]^2 \tag{10}$$

where m and n are the dimensions of the image, and i and j are the pixel locations.

3.2. Real CT data

We obtained two sets of raw projection data from an industrial CT system. One set of data was derived from a polymethyl methacrylate object with a relatively low density (Fig. 7), and the other set of data was derived from an aluminum object with a relatively high density (Fig. 8). As shown in Fig. 7, the first real data set (Real Data 1) was acquired using a cone-beam CT system, from SEC, with a 2048 × 2048 FPD. This data set encompassed 400 total views, over a range of 360 degrees. The detector element was 0.198 mm in width, the source-axis distance (SAD) was 193.978 mm, and the source-detector distance (SDD) was 915 mm. The second real data set (Real Data 2) was also projected as 200 views per full-scan. Each scan was obtained from a CBCT scanner, with 1200 × 1200 FPDs, as shown in Fig. 8. In this data set, the detector bins were 0.085 mm in width, the SAD was 65 mm, and the SDD was 500 mm.

4. Results

4.1 Simulation studies

The numerical phantoms used to evaluate the efficiency of ring artifact removal in a simulation study are shown in Figs. 3-5. The ground truth images are shown in (a) of Figs. 3-5, whereas the ring artifact images with different ring patterns and strengths are shown in (b). The compensated images generated by the MA, MedF, and line-ratio methods, respectively, are shown in (c)-(e). The profiles of all compensated images are shown in (f) of Figs. 3-5, in order to easily compare these images. All profiles were extracted from the white line in each figure, which is designated with an arrow.

The compensated image generated by the MA method, shown in (c), exhibits a reduced number of ring artifacts compared with the original image; however, the image also contains wide and fluctuating rings that did not exist in the original ring artifact image (b). This observation may reflect another artifact that makes identification or judgment of the image difficult. The image generated after application of the MedF method, shown in (d), shows that the MedF method performed better than the MA method with respect to removal of the original rings. Moreover, the MedF method generated less additional artifacts than the MA method. However, neither of these methods could effectively correct images without introducing additional artifacts. The additional artifacts in MA- and MedF-compensated images presumably result from the specific limitation of these approaches, namely, only the mean curve is used to identify and to compensate for defective detector elements [12,13].

#208844 - $15.00 USD Received 25 Mar 2014; revised 19 May 2014; accepted 20 May 2014; published 27 May 2014

These two conventional methods calculate the mean curve, then remove the peaks from this mean curve. However, the shape of the actual mean curve varies according to the density and components of the object being imaged. Therefore, by changing the density and/or the shape of the object, the mean curve could contain peaks that do not cause ring artifacts. The MA and MedF methods remove all peaks, including the peaks originating from the density and specific components of the object. Thus, these methods cannot accurately distinguish whether a peak actually originates from the ring artifact or whether additional artifacts have been introduced.

Compared with the two conventional methods, the line-ratio method (e) exhibited the best performance. The line-ratio method effectively removed ring artifacts without introducing additional artifacts. Although the profiles of images generated using the MA and MedF methods (f) show that many peaks resulting from ring artifacts were suppressed, these images still exhibited ring artifacts. Moreover, these images differed considerably from the ideal profile without ring artifacts, and these differences led to the introduction of additional artifacts into the images. In contrast, ring artifacts were effectively removed with the line-ratio method; moreover, the line-ratio method did not introduce any additional artifacts. The line-ratio method can therefore remove peaks from ring artifacts; moreover, the profile of the image generated by the line-ratio method was almost identical to that of the ideal profile.

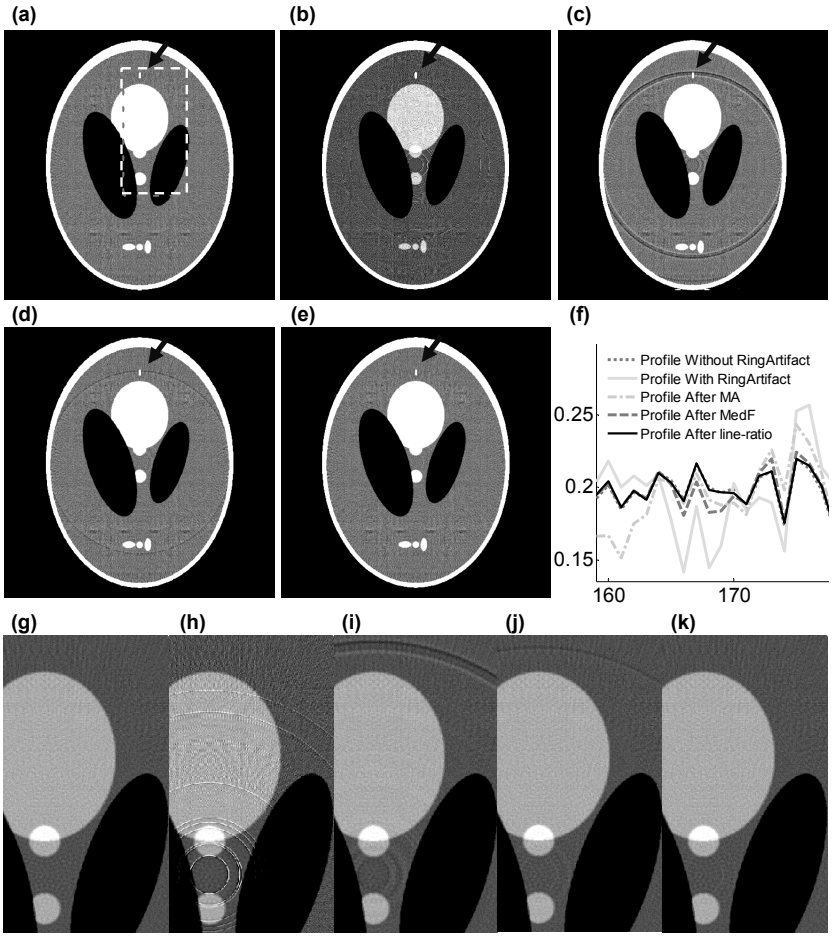

Fig. 3. Comparative results of ring artifact reduction after applying synthetic phantom 1. (a) Without ring artifacts, (b) with ring artifacts, (c) after the MA method, (d) after the MedF method, (e) after the line-ratio method, (f) profiles of each method, and (g)-(k) are the magnified views of the boxed area in (a)-(e), respectively.

#208844 - $15.00 USD Received 25 Mar 2014; revised 19 May 2014; accepted 20 May 2014; published 27 May 2014

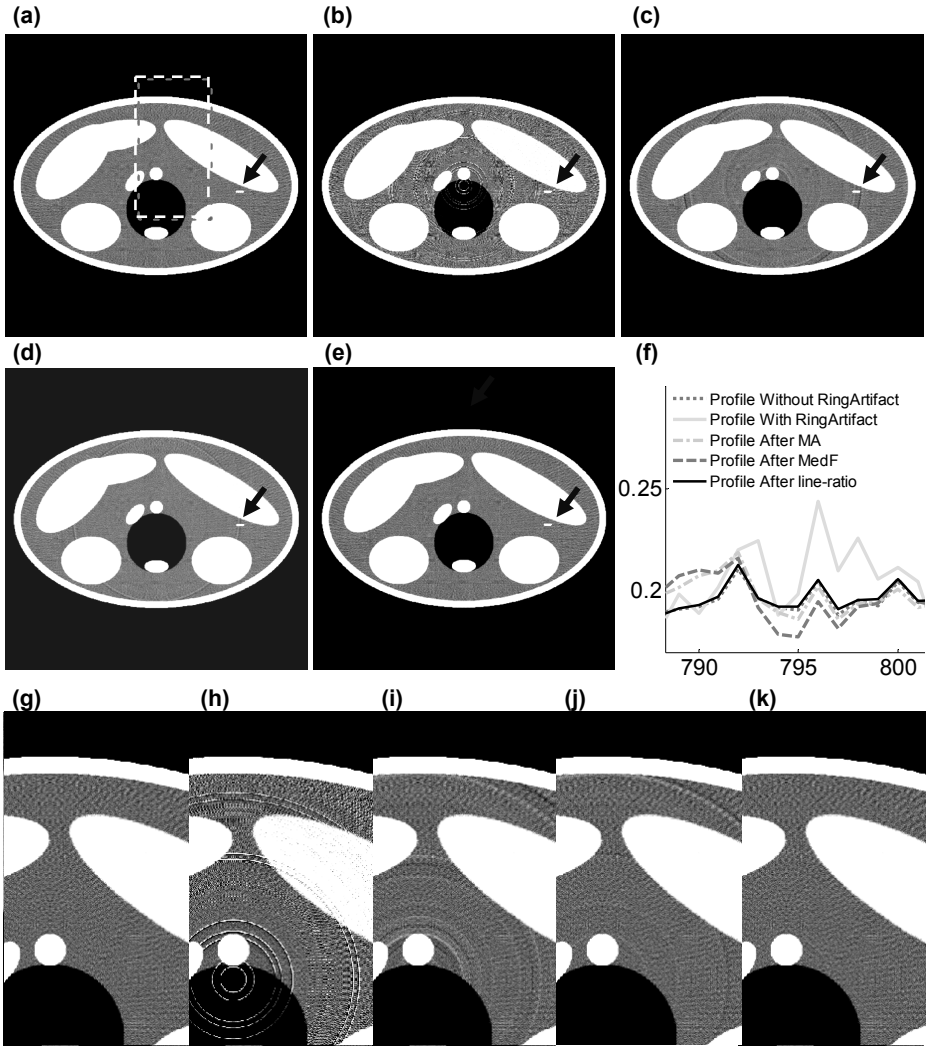

Fig. 4. Comparative results of ring artifact reduction after applying synthetic phantom 2. (a) Without ring artifacts, (b) with ring artifacts, (c) after the MA method, (d) after the MedF method, (e) after the line-ratio method, (f) profiles of each method, and (g)-(k) are the magnified views of the boxed area in (a)-(e), respectively.

#208844 - $15.00 USD Received 25 Mar 2014; revised 19 May 2014; accepted 20 May 2014; published 27 May 2014

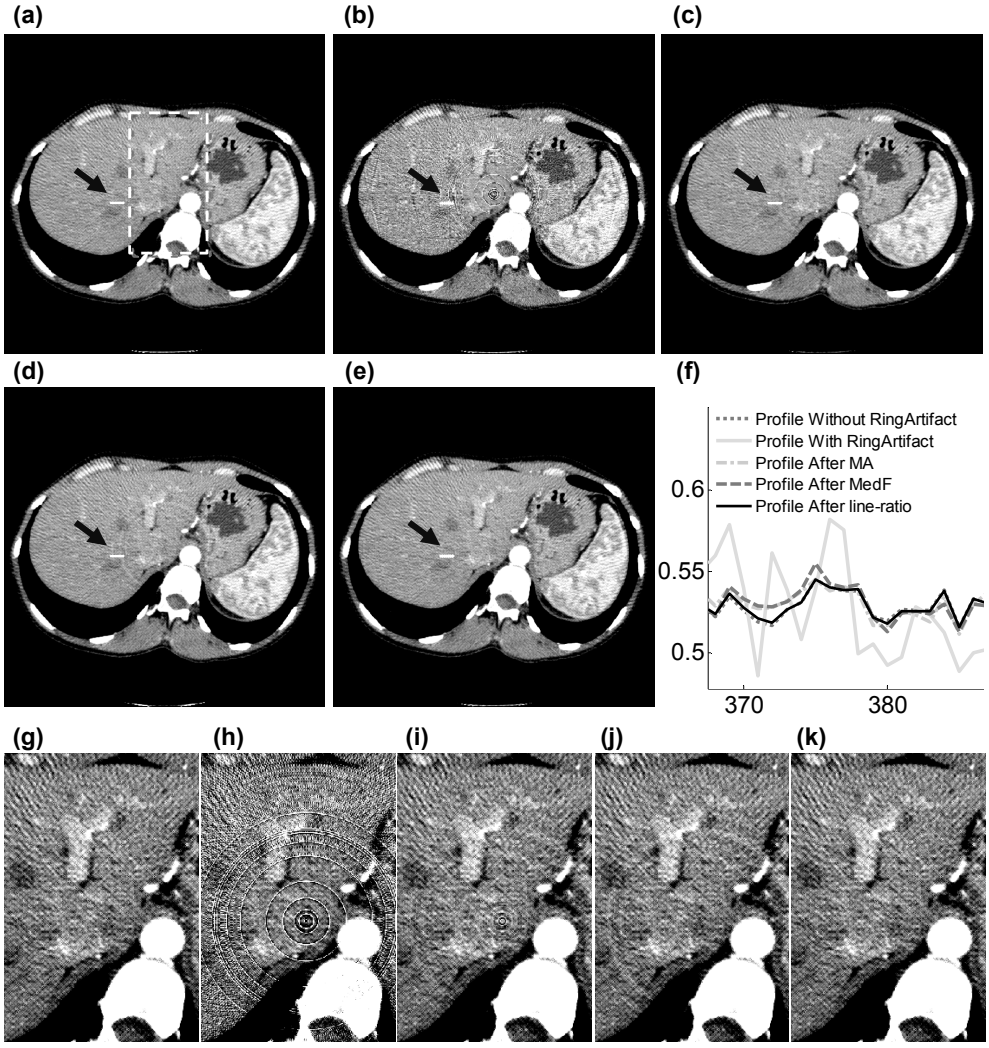

Fig. 5. Comparative results of ring artifact reduction after applying synthetic phantom 3. (a) Without ring artifacts, (b) with ring artifacts, (c) after the MA method, (d) after the MedF method, and (e) after the line-ratio method. (f) Profiles of each method. (g)-(k) are the magnified views of the boxed area in (a)-(e), respectively.

For quantitative analysis, the MSE values were calculated from all simulation data shown in Table 1 (Fig. 6). The line-ratio method performed better for all simulation data than either the MA method or the MedF method.

Table 1. Performance Comparison of Different Methods in Terms of the MSE

Simulation Data	MSE		
	MA method	MedF method	Line-ratio method
Synthetic Phantom 1	7.10E-05	2.35E-06	7.13E-07
Synthetic Phantom 2	2.05E-05	3.54E-06	1.00E-06
Synthetic Phantom 3	1.69E-05	1.60E-05	2.67E-06
Average	3.61E-05	7.28E-06	1.46E-06

#208844 - $15.00 USD Received 25 Mar 2014; revised 19 May 2014; accepted 20 May 2014; published 27 May 2014

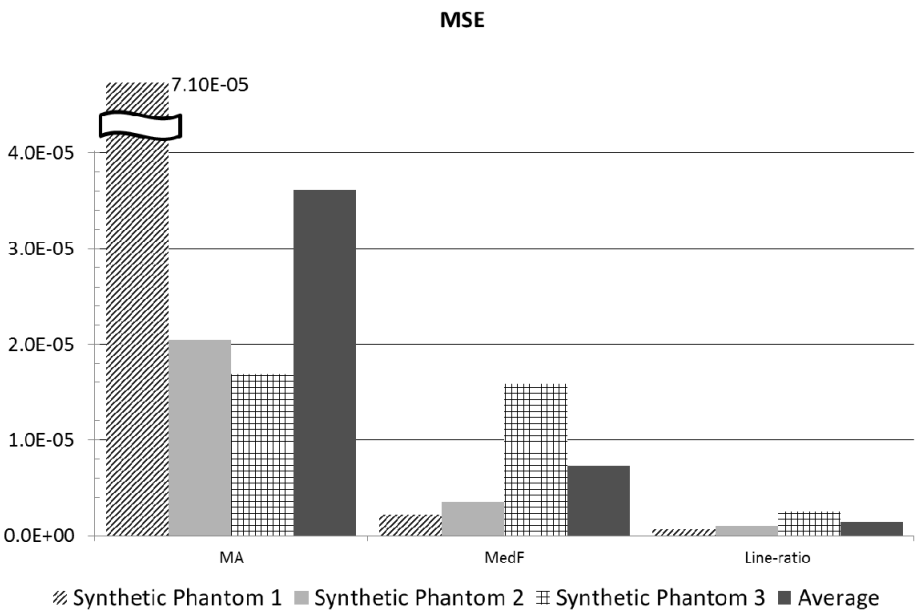

Fig. 6. MSE values for each method.

4.2 Resulting images from real CT data

Each ring artifact removal algorithm was applied to real CT data (Figs. 7 and 8). The ring artifact images (a), images after the MA method (b), images after the MedF method (c), and images after the proposed line-ratio method (d) are shown in Figs. 7 and 8. To facilitate image comparison, the same region of interest (ROI) in the center of each image was used (e).

The MA and MedF methods are capable of slightly reducing the number of ring artifacts; however, neither of these methods is able to remove serious artifacts. The MA and MedF methods were also unable to remove wide and/or fluctuating rings, such as those depicted in the ring artifact image shown in Figs. 7(a) and 8(a). This failure to remove certain types of rings is probably due to the fact that the MA and MedF methods remove the peaks in the mean curve to compensate for ring artifacts. As previously discussed, this peak removal process is not sufficient to identify, and compensate for, differences in detector sensitivity. Therefore, wide and/or fluctuating rings can remain, as shown in Figs. 7 and 8(b), (c).

As shown in Figs. 7(d) and 8(d), the line-ratio method removes ring artifacts more effectively than the conventional methods. Unlike the MA and MedF methods, the line-ratio method removes rings uniformly, without introducing additional artifacts. The line-ratio method also cleanly removes ring artifacts, even very strong ring artifacts. The degrees of ring artifact removal by the line-ratio method and the conventional methods are demonstrated in the magnified images shown in Fig. 7(e) and 8(e), which facilitates comparison of the three methods and clearly shows that the line-ratio method is superior. The profiles extracted from the line designated with an arrow in each image also illustrate which method is best for removing ring artifacts, as shown in Figs. 7(f) and 8(f).

#208844 - $15.00 USD Received 25 Mar 2014; revised 19 May 2014; accepted 20 May 2014; published 27 May 2014

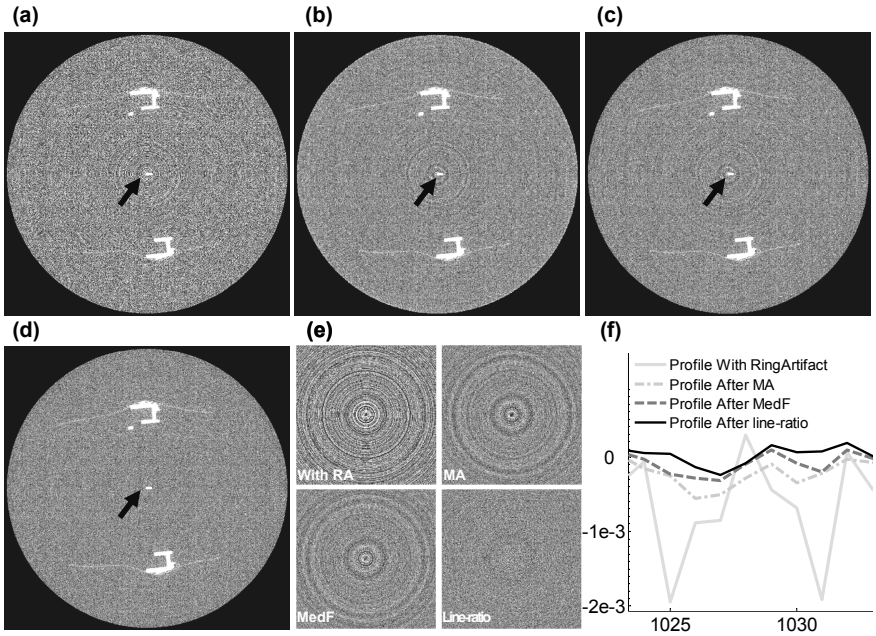

Fig. 7. Comparative results of ring artifact reduction on the first real data set (Real Data 1) (a) with ring artifacts, (b) after applying the MA method, (c) after applying the MedF method, and (d) after applying the line-ratio method. (e) Magnified images of (a)-(d). (f) Profiles of each method.

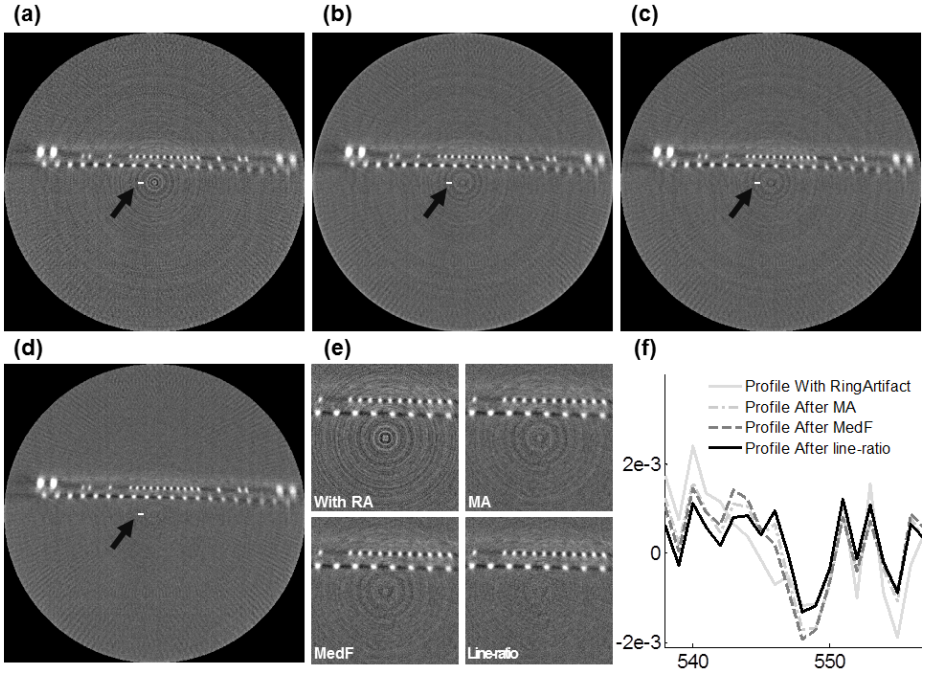

Fig. 8. Comparative results of ring artifact reduction on the first real data set (Real Data 2) (a) with ring artifacts, (b) after applying the MA method, (c) after applying the MedF method, and (d) after applying the line-ratio method. (e) Magnified images of (a)-(d). (f) Profiles of each method.

#208844 - $15.00 USD Received 25 Mar 2014; revised 19 May 2014; accepted 20 May 2014; published 27 May 2014

4. Conclusion

The non-uniform sensitivity of detector elements is known to introduce ring artifacts into reconstructed CT images. While several methods have been developed to remove ring artifacts, the performances of these methods are object-dependent, and therefore these methods are not optimal solutions. The MA and MedF methods are also insufficient for reducing ring artifacts, because the mean curves used in the MA and MedF methods cannot adequately deal with the large differences in sensitivity between various detector elements. While the iterative approach developed in [18] removed ring artifacts more effectively than these two methods, the iterative approach was computationally laborious, since it entailed searching for a correction factor until a certain criterion was satisfied. In addition, the computation time was shown to increase with the number of detector channels.

In contrast, the line-ratio method proposed here approaches the ring artifact problem fundamentally and efficiently, by taking into account variations in detector sensitivity. Moreover, our method is relatively simple and effective compared with other iterative methods, since it does not use an iterative process or need to satisfy a stop criterion. Another advantage of our method is its robustness for handling noise. In real data with noise, our method clearly removed the ring artifacts, as shown in Figs. 7 and 8.

Here, we tested and compared the line-ratio method with two conventional methods, the MA method and the MedF method. We verified the effectiveness of the line-ratio method and validated its performance with both synthetic and real data. We found that the line-ratio method was more effective and more adaptive in removing ring artifacts than either the MA method or the MedF method. Compared with conventional methods, the MA method and the MedF method, our proposed method offers superior performance for effectively removing ring artifacts.

Acknowledgments

This work was supported by the IT R&D program of MKE/KEIT. [10043897, Development of 500 cGy level radiation therapy system based on automatic detection and tracing technology with dual-head gantry for 30% reducing treatment time for cancel tumors], Basic Science Research Program through the National Research Foundation of Korea (NRF) funded by the Ministry of Education, Science and Technology (2012-0008577), and SEC Co., Ltd.

#208844 - $15.00 USD Received 25 Mar 2014; revised 19 May 2014; accepted 20 May 2014; published 27 May 2014